Metals and Materials International (2024) 30:1209–1226
https://doi.org/10.1007/s12540-023-01574-9

Characterization and Microstructure of Recycled Eroded Particles from Die-Sink Electro Discharge Machining of H11 Alloy for Applicability in Additive Manufacturing

Oliver Voigt[1] · Marco Wendler[2] · Asim Siddique[1] · Hartmut Stöcker[3] · Caroline Quitzke[2] · Urs A. Peuker[1]

Received: 12 July 2023 / Accepted: 6 November 2023 / Published online: 16 December 2023

Abstract
Different waste streams from electro discharge machining (EDM) were investigated for an upcycled usage in processes for additive manufacturing (AM). These erosion sludges accumulate in filter cartridges and at the bottom of machining basins. The enclosed particles were extracted, sieved and investigated via laser diffraction, dynamic image analysis, scanning electron microscopy, optical emission spectroscopy, elemental analysis and flowability measurements. Additionally, thermal, crystallographic and metallographic investigations as well as X-ray micro-computed tomography (µ-CT) were utilized for the characterization of particle and material properties. In general, eroded powders fulfill the requirements for AM regarding particle size and shape very well, which is confirmed in morphological investigations and powder flow characteristics showing similar properties as the H11 AM reference material. The chemical composition of the powders is equal to the machined H11 alloy, except for the high carbon content. Carbon is entrapped in the iron lattice originating from pyrolysis of the present dielectric fluid and the graphite electrode during rapid solidification, which leads to a transition from martensite to cementite structures. This change is observed in the microstructure of powders, in which acicular primary cementite and austenite are present. After remelting with slow heating and cooling rates the microstructure changed to ledeburite II with retained austenite and martensitic phases. The pore size and shape distributions obtained by µ-CT measurements showed a pore formation in the compact sample. These results provide a fundament of major properties as well as handling and recycling suggestions for eroded particles enclosed in waste sludges.

Keywords Electro discharge machining · Particle characterization · Particle properties · Microstructure · Additive manufacturing · Recycling

1 Introduction

The commonly used electro discharge machining (EDM) is a technique to postprocess metallic and/or electrically conductive components for achieving desired shapes or textures with a defined material removal [1, 2]. EDM techniques are based on an erosive character of electrical discharges between two electrodes in a dielectric fluid. Thereby, a conversion from electrical into thermal energy leads to the material removal. Nowadays, the two predominant techniques are die-sink EDM and wire EDM [1, 3], which are important for sectors within the mold and construction industry for implementing features with high aspect ratios or bigger cavities and slots. Mostly, different types of die or hot work steels, which have in general a martensitic microstructure, are processed with both techniques. The main differences are the used dielectrics on the one hand, and the tool electrode material as well as geometry on the other hand. In wire EDM a brass or copper wire is used as an electrode, whereas in die-sink EDM mostly graphite electrodes are common. These processes are performed in deionized water (wire) and synthetic hydrocarbon oil (die-sink), respectively [4, 5]. In this study, the focus lies on die-sink EDM and its waste

✉ Oliver Voigt
oliver.voigt@mvtat.tu-freiberg.de

[1] Institute of Mechanical Process Engineering and Mineral Processing, Technische Universität Bergakademie Freiberg (TUBAF), Agricolastraße 1, 09599 Freiberg, Germany

[2] Institute of Iron and Steel Technology, TUBAF, Leipziger Straße 34, 09599 Freiberg, Germany

[3] Institute of Experimental Physics, TUBAF, Leipziger Straße 23, 09599 Freiberg, Germany

streams operating with a graphite tool electrode and a martensitic hot work steel as the workpiece electrode, which is quite often H11 alloy.

In contrast, the sector of additive manufacturing (AM) gains more attention and a greater influence in several industries due to some major advantages [6, 7]. However, AM powders are expensive due to their tight specifications regarding particle size distribution (PSD), circular/spherical shapes, chemical composition, allowable number of defects as well as flowability and bulk mechanics [8–10]. Particle sizes in the range from 15 to 60 µm with a median particle size $x_{50,3}$ of around 30 µm are used in selective laser melting (SLM) [9, 11] and sizes from 60 to 100 µm, max. 125 µm, with a $x_{50,3}$ of 70 to 80 µm for the electron beam melting (EBM) [12, 13] process. Apart from that, the process of Binder Jetting (BJT) [14, 15] and direct energy deposition (DED) [16, 17] should also be taken into account, where various metal-based powders of different and/or bimodal PSD are used. Moreover, a low number of defects, good flowability characteristics as well as high circularities and sphericities of the powders are required for the formation of a homogenous powder layer to achieve good qualities of printed parts [18, 19]. A checking on crystallographic information of appearing structures, lattices and phase fractions is another quality assurance tool for characterizing generated powders. Metallographic investigations of metallic samples, compact parts or powders, respectively, are important regarding their microstructure since this is influencing the manufacturing process itself and the final parts properties.

The main reason for the high costs of AM powders is the production. Nowadays, there is only the opportunity to manufacture powders via the cost and energy intensive process of powder atomization of metal melts [20, 21]. In Germany the costs for raw materials in AM industry amount to approx. 50% of the total manufacturing costs, according to the Federal Statistical Office [22]. Therefore, it is indispensable to focus on alternative ways of supplying metal powders. Current works related to this topic are mostly different recycling strategies for used powders to increase the resource efficiency. Most commonly, used powders with an undefined number of processed cycles in the AM chamber get manufactured again with or without creating mixtures in different ratios with virgin powder. For SLM it is reported, that a powder reuse comes along with changes in physical (particle fusion and agglomerates) and chemical (contaminations) properties caused by heat conduction and spatters in the powder bed degrading the powder layer [23]. Lu et al. compared virgin and recycled 316L powder in SLM over several cycles and found an increase of coarser particles (particle spatter, fusion) with higher circularities and hardness in general [24]. Moreover, the microstructure remains unaffected, whereas a slight change in the crystal structure and a significant increase of the oxygen content was observable. Rayan et al. investigated a maraging steel powder in SLM over several cycles leading to coarser particles and a degradation of the particle shape, but no changes in the bulk density [25]. Besides that, tensile properties and fatigue behavior of printed parts are slightly affected with simultaneously more internal defects due to lack of fusion, gas entrapments and carbon inclusions.

Looking on powder recycling conducted for EBM devices, Popov et al. reported for recycled Ti-6Al-4V powders a formation of various defects leading to deteriorations of mechanical properties and the fatigue behavior, but unaffecting the developed microstructure [26]. In contrast to that, Tang et al. found for the same material after a reuse of 21 cycles in EBM a better flowability of the powders as well as no significant influences on mechanical properties in manufactured components [27]. For H11 powder no detailed studies of powder recycling could be found. Another study by Richter et al. investigated the mechanical recycling of Ti-6Al-4V parts for providing secondary powders. Therefore, molten and sintered support structures were comminuted in a hammer mill and mixtures of these obtained powders with virgin powder were processed via EBM [28]. This stays in contrast to the recycling of unmolten powders mentioned above. In general, some powder mixtures can meet the mechanical properties and fatigue behavior of reference specimen only affected by an iron contamination of the milling tools due to mechanical alloying.

Another approach to achieve the matter of reducing raw material costs and energy consumption is the secondary usage of waste streams from EDM. Thereby, a certain amount of erosion sludge accumulates and is collected in filter cartridges or can be found at the bottom of the working basin. Considering the enclosed particle sizes as well as shapes, it could be stated, that some requirements can be fulfilled quite easily [29, 30]. Besides that, the EDM mechanism can be a useful tool for a customized synthesis of powder particles [31]. Thus, any aspects of a recycling of these EDM wastes are not under investigation. Currently, generated waste sludges and filter cartridges are collected and getting directly disposed for metallurgical processes or smelting. In this paper, a holistic characterization of enclosed eroded particle systems from sludge in filter cartridges and sludge from the basin bottom is performed to give detailed information about eroded particles and their applicability in AM-processes. Characterizations of the particle size, particle morphologies, chemical composition and bulk powder properties for different size classes as well as structural information about occurring crystal lattices and possible transitions are discussed. Analyses of the particle microstructure as well as the developed microstructure and inner structure after remelting is presented to derive information for further application fields. All results are presented to

highlight an opportunity of recycled eroded particles as a secondary raw material for applicable processes in AM.

2 Materials and Experimental Setup

2.1 Waste Streams and Reference Material

Investigated EDM waste streams have to be distinguished into two different types, which are sludges from the bottom of the machining basin and sludges enclosed in filter cartridges. As a tool electrode 99.9% graphite was used combined with a commercially hydrocarbon-based, synthetic dielectric. The machining parameters are unknown. The samples are named as ES1 (ES = erosion sludge; from basin, Fig. 1a–c), ES2 from filter cartridge type A (Fig. 1d–f) and ES3 from filter cartridge type B (Fig. 1g–i). Cartridges have cylindrical geometries with diameters and heights of 50 cm × 30 cm and 35 cm × 15 cm, respectively, with weights of 6 kg to 27 kg. Yields of processable sludges differ strongly from 1.5 to 5.5 kg for ES2/ES3 compared to around 50 kg ES1 sludge.

A frequently used steel alloy in EDM as well as in AM is the martensitic hot work steel H11 (1.2343/X37CrMoV5-1) and is characterized by a high tensile and yield strength, ductility, wear resistance, thermal shock resistance and thermal conductivity according to data sheets. This alloy features a high density and a very high relative density of AM parts (< 99.9%) [32] with a carbon content between 0.33 and 0.43 wt% located in the hypoeutectoid range. This commercially available and gas atomized (Ar) powder was chosen as the reference material (GKN Powder Metallurgy, GKN Hoeganaes Corporation Europe, Buzau, Romania) because components made out of this alloy got machined via die-sink-EDM in the supplying companies.

2.2 Particle Extraction

In general, sludge consists of three components, which are the oily phase, particles from the tool electrode—graphite—and particles from the workpiece electrode—metallic particles. To extract the particles from the sludges, the oil phase has to be dissolved. Therefore, acetone (≥ 99.5%, Carl Roth GmbH and Co. KG, Karlsruhe, Germany) is used as an organic solvent. The suspension gets filtered, centrifuged and decantated due to the sedimentation behavior of dense metallic particles resulting in two fractions (lighter ones—graphite; heavier ones—metals). A vacuum pump, a self-constructed filter pressure groove and a centrifuge (Megafuge ST1R plus with a rotor F15-6X100 FIBERLITE carbon fiber, Thermo Fisher Scientific Inc., Waltham, MA, USA) were used for particle extraction. Afterwards, particles are dried in an oven overnight at 80 °C. The de-oiled particles were sieved (20 µm; 63 µm; 125 µm) with a sieving device (AS 200 Control g, Retsch GmbH, Haan, Germany) for 10 min.

2.3 Characterization of Particle Systems

2.3.1 Particle Size, Shape and Morphology

The raw sludges were suspended in isopropanol (≥ 99.5%, Carl Roth GmbH and Co. KG, Karlsruhe, Germany) with ultrasonic treatment (3 min, 50% amplitude) and were measured in cuvette R3 via laser diffraction (HELOS, Sympatec GmbH, Clausthal-Zellerfeld, Germany). Following

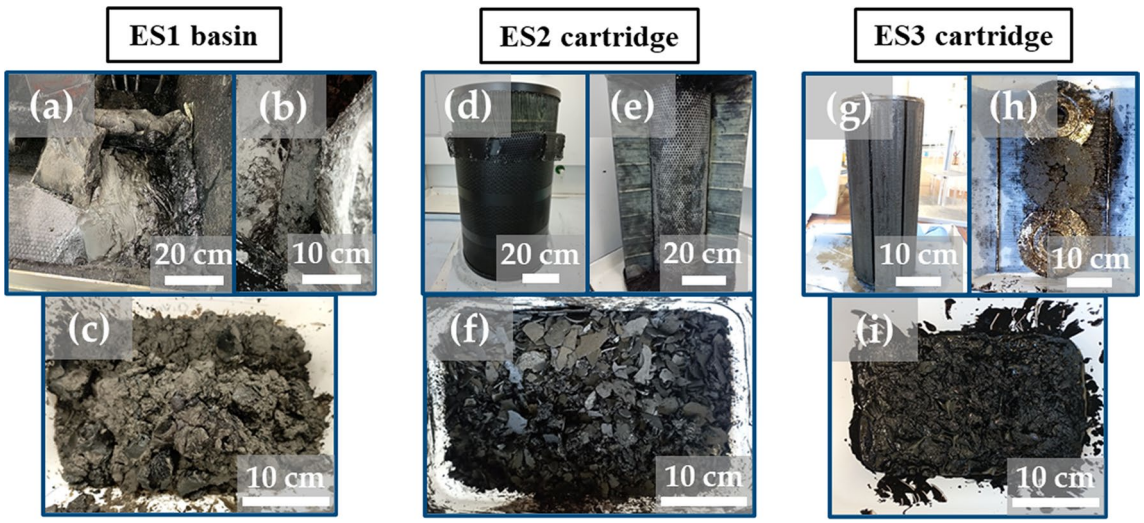

Fig. 1 Received EDM waste streams: sludge from the basin ES1 (**a**–**c**); filter cartridge A before and after dismantling (**d**, **e**) with obtained sludge ES2 (**f**) and filter cartridge B before and after dismantling (**g**, **h**) with obtained sludge ES3 (**i**)

characterizations were performed on dry particles after extraction. Measurements in laser diffraction (R3) in isopropanol and dynamic image analysis in deionized water (HELOS and QICPIC LIXELL, both Sympatec GmbH, Clausthal-Zellerfeld, Germany) were carried out to quantify particle size and shape factors. Images of the particle morphologies were taken via a desktop SEM (with 10 kV; Phenom, FEI/Thermo Fisher Scientific Inc., Waltham, MA, USA) with BSE imaging.

2.3.2 Chemical Composition

A standard solution for optical emission spectroscopy with inductively coupled plasma (ICP OES; iCAP 6300, Thermo Fisher Scientific Inc., Waltham, MA, USA) was calibrated with the alloy elements Cr, Cu, Fe, Mn, Mo, Ni, P, Si, V (solutions obtained from Carl Roth GmbH and Co. KG, Karlsruhe, Germany). Before measuring, samples were dissolved and boiled in aqua regia. Carbon and sulfur contents were measured using a G4 Icarus C-S-Analyzer (Bruker AXS GmbH, Karlsruhe, Germany). Thereby, the sample was combusted in an oxygen stream and measured with two infrared detectors after calibration with certified steel reference material (AR 304). Oxygen contents were measured in G8 Galileo O-Analyzer (Bruker AXS GmbH, Karlsruhe, Germany) by degassing the samples during melting in a graphite crucible and detecting via infrared detectors, after equal calibration.

2.3.3 X-ray Diffraction

X-ray diffraction (XRD) of the samples H11 and ES1 20–63 µm was used to determine phase fractions including the role of carbon. The coarser fraction ES1 63–125 µm should not differ significantly from its smaller size fraction. The measurements were carried out on a D8 Advance diffractometer (Bruker Corporation, Billerica, MA, USA) using Cu-$K\alpha$ radiation. The powders were prepared on plastic sample holders of 25 mm diameter and irradiated with a variable slit set to a constant illuminated length of 20 mm. The diffracted intensities were collected with a Bruker LynxEye XE-T silicon strip detector in high-resolution mode to suppress all wavelengths except Cu-$K\alpha_{1/2}$. Radial and axial soller collimators were used to improve the signal-to-noise ratio and the peak shape, respectively. The diffraction patterns were evaluated by Rietveld analysis using the program Bruker Topas version 6. Measurements were carried out in air under ambient pressure at room temperature.

2.3.4 Bulk Powder Properties

For properties of the bulk powders, density measurements of the fractions and reference powder were carried out in a gas pycnometer (AccuPycII; micromeritics GmbH, Unterschleissheim, Germany). Moreover, bulk as well as tap densities were obtained via measurements in a bulk funnel (SMG 697, Powtec Maschinen und Engineering GmbH, Remscheid, Germany) with a 500 mL vessel and a tamping volumeter (JEL StavII, J. Engelsmann AG, Ludwigshafen, Germany) in a cylinder with a volume of 100 mL. With the ratio of both values the Hausner number was calculated, which is an indicator of the flow behavior. Apart from that, flow times of the three powders in a Hall flowmeter out of a Hall and Carney funnel (NanoTech Industrie Produkte, Berlin Germany) were determined.

2.3.5 Microstructure of Particles

Metallographic investigations were performed in a light microscope Axio Observer Z1m (Carl Zeiss AG, Oberkochen, Germany) on both sieved powder fractions to obtain information about the particle microstructure after solidifying in the dielectric. Particles were embedded in Polyfast (bakelite with carbon filler; Struers LLC, Cleveland, OH, USA), ground with SiC-paper and polished with diamond suspension (3 µm) and colloidal SiO_2 (0.04 µm; both Struers LLC). Finally, the samples were etched in Nital (2% HNO_3) or Pikral (4% $C_6H_3N_3O_7$; both Struers LLC). Additionally, the microstructure was examined using a Ultra55 field emission electron microscope (FESEM; Carl Zeiss AG, Oberkochen, Germany). Electron backscatter diffraction (EBSD) measurements were conducted using an OIM XM4 system (AMETEK GmbH, Unterschleissheim, Germany) and evaluated with OIM AnalysisTM V8 software from AMETEK. An accelerating voltage of 20 keV and a step size of 0.08 µm were used for the EBSD investigation. The sample was prepared similarly, but got end polished on a vibratory polisher (VibroMet2; Buehler Group, Uzwil, Switzerland) for 24 h and remained unetched.

2.3.6 Preparation of Solid Sample and Developed Microstructure

Thermogravimetric analysis (TGA; STA 443 F3 Jupiter, Netzsch GmbH and Co. KG, Selb, Germay) was conducted on powder sample ES1 < 125 µm to get a compact solid sample for metallographic investigation. The powder was melted in N_2 atmosphere up to 1500 °C with a heating rate of 10 K min^{-1} followed by uncontrolled oven cooling. The TGA measuring cell was connected to a vapor phase Fourier-transform infrared spectrometer (FTIR; Tensor 27, Bruker Corporation, Billerica, Massachusetts, USA) to analyze the evaporating gases and check for hydrocarbon oil residues. The compact sample was embedded in Durofast (epoxy with mineral filler; Struers LLC), ground with SiC-paper, polished with diamond suspension (3 µm) and colloidal SiO_2

(0.04 µm; both Struers LLC) and finally etched in Nital for investigations via a light microscope Axio Observer Z1m (Zeiss).

2.3.7 µ-CT Measurements

Before embedding the TGA tablet, investigations in a µ-CT device (Xradia 510 Versa, Carl Zeiss AG, Oberkochen, Germany) were conducted to reveal the inner structure and correlated to the metallographic analyses for the examination of the internal porosity or occurring voids after resolidifying. The sample was fixed with UV-hardening epoxy resin on a wooden stick. One overview and one high-resolution scan (in the inner region) were carried out, respectively. An overview scan of the whole sample was performed to see the pore distribution in the whole sample and to identify a region of interest (ROI) for the high-resolution scan. The scan settings used for both µ-CT measurements are listed in Table 1.

The reconstruction (Fig. 2) of both µ-CT scans was performed in the Zeiss reconstruction software and for the image processing, segmentation and analysis ORS Dragonfly (Object Research Systems, Montréal, Québec, Canada) software was used. Further image processing and pore analysis were conducted on the high-resolution scan. The denoising of the images was carried out with the Gaussian filter [33], by setting the kernel size to 5, Standard distribution to 0.7 and by keeping the unit size to 16 of the input data. The segmentation of the pores was performed for the quantification of the pore size and shape. Due to the variation in the pore sizes and their greyscale values the segmentation was performed by using the U-net segmentation model [34]. To train the segmentation model few slices were added by hand-labeling the pores and the remaining sample area.

Table 1 Scan settings of the µ-CT measurements for the overview and high-resolution scan of sample ES1 < 125 µm

Parameter	Overview scan	High-resolution scan
Acceleration voltage (keV)	160	140
Power (W)	10	8
Optical magnification	0.4	4
Exposure time (s)	1	15
Voxel size (µm)	5.78	1.34
Number of projections	1601	1601
Binning	2	2
Source filter	Zeiss standard HE3	Zeiss standard HE3

3 Results and Discussion

3.1 Particle Size and Shape

The composition of the individual sludges regarding the oil and solid content differs strongly. For ES1 around 85 wt% represent solid particles and 15 wt% the dielectric fluid, whereas in filter cartridges the oil phase reaches values of approx. 65 wt% to 80 wt%, which could be calculated from filtration and centrifugation experiments as well as TGA measurements. Figure 3a illustrates the PSD of all three raw sludges. It is conspicuous, that both sludges out of the filter cartridges (ES2 and ES3) have a very high fine fraction. Their $x_{50,3}$ values are very low with 1.5 µm and 1.6 µm,

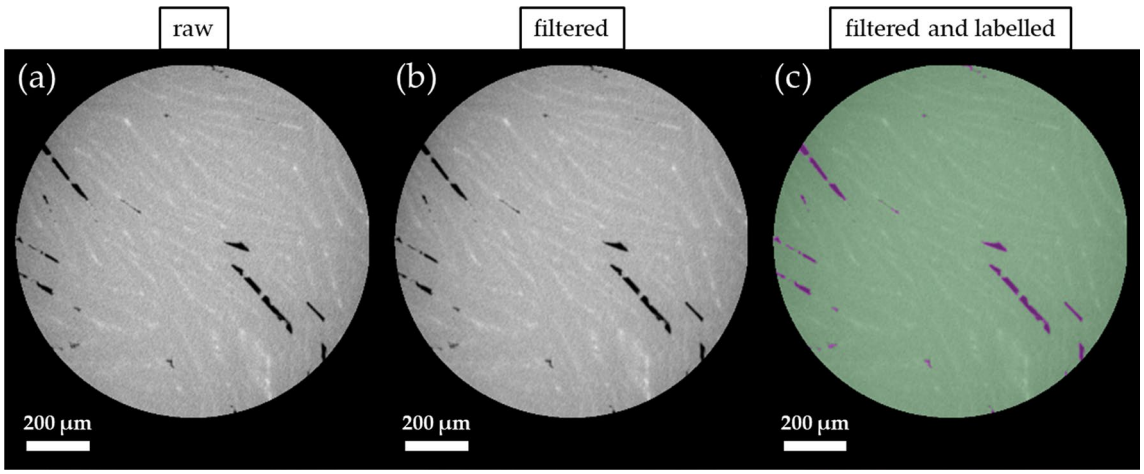

Fig. 2 µ-CT slices of TGA–DSC sample ES1 < 125 µm of high-resolution scan after manual reconstruction and segmentation; (**a**) raw image; (**b**) processed image with Gaussian filter for noise reduction; (**c**) labeled image distinguishing between matrix (green) and pores (purple) after deep learning algorithm

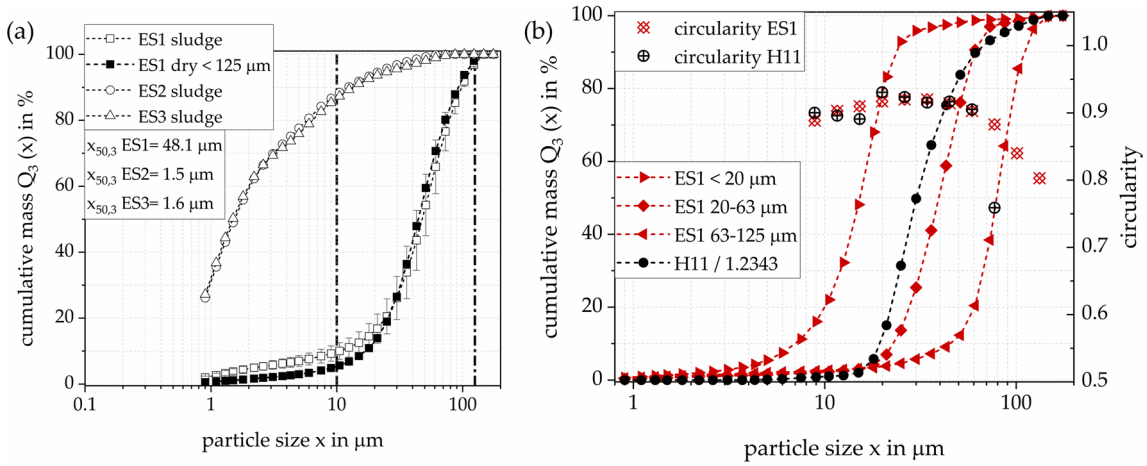

Fig. 3 PSD obtained from laser diffraction dispersed in isopropanol with ultrasonic treatment of the three erosion sludges in the initial state and of dry powder from basin sludge ES1 < 125 µm (**a**) and of three sieved eroded powder fractions < 20 µm, 20–63 µm, 63–125 µm as well as exemplary H11/1.2343 reference powder and their circularity values (**b**)

respectively. When considering the minimal particle sizes for AM-processes, the yield of suitable particles larger than 10 µm is low with 15 wt%. Furthermore, the content of less dense graphite is very high and metallic particles amount just to approx. 10 wt%. High amounts of bigger (metallic) particles are not located in the cartridges due to the built-in fine fabrics, therefore, sludges from filter cartridges cannot be considered and processed sustainable. In contrast to that, the PSD of basin sludge is significantly different and shifted to coarser particle sizes covering at least three different ranges for possible AM techniques. Bigger, and thus heavier high dense metallic particles settle relatively fast to the basin bottom after congealing in the dielectric fluid, where they cannot reach the step of filtration and get collected afterwards.

Figure 3b shows the PSD of the sieved fractions and H11 including circularity values from dynamic image analysis. Sieving into these fractions was chosen due to the usage of different size classes depending on the AM-process. In perspective, fractions 20–63 µm for SLM and 63–125 µm for EBM, respectively, should be tested. Both fractions will be investigated for BJT and DED, as well, or with alternatively sieved fractions. Comparing the SLM-suited fraction with the SLM powder, no significant differences are observed, except a slight shift to bigger particle sizes, which can be seen in the $x_{50,3}$ value of 30.1 µm (H11) and 39.5 µm (ES1 20–63 µm), respectively. Both powders show a narrow and normally distributed PSD with constantly high circularity values of 0.92 (H11) and 0.91 (ES1 20–63 µm). For H11 powder a slight decrease in the circularity values at bigger particle sizes is observable, which can result from particle fusion processes during powder atomization. A similar trend can be seen for the EBM-suited fraction as well, which has a lower circularity of 0.89, probably due to more particle fusion occurrence, and a $x_{50,3}$ of 79.3 µm. High circularity values were expected and are the consequence of the high temperature gradients and rapid solidification leading to circular shaped particles due to energetically best, low surface tension forces [35, 36]. Overall, eroded particles fully fulfill the requirements regarding particle size and shape.

3.2 Dynamic Image Analysis

Figure 4 shows 2D kernel density estimation plots [37] (KDE; created in OriginPro Software) for the relevant particle properties of H11 reference (a) as well as eroded powders ES1 20–63 µm (b) and 63–125 µm (c) regarding the EQPC (diameter of area equivalent circle) and circularity. In general, it is a non-parametric procedure for probability density functions (PDF) with the goal to derive the PDF everywhere including domains, where no data points are existing. Therefore, finite samples of data are accessed, which means utilizing two independent particle properties to achieve a 2D kernel density map. For each KDE, up to 500,000 particles were evaluated.

For eroded powder fractions it is visible, that the used upper and lower sieving cuts were implemented quite well. For the smaller sized fraction, lower circularity limits are observable, which could result from agglomeration and particle fusion of the smallest, vaporized particles with lowest values around 0.75. The coarser fraction shows slightly higher circularity values (minimum 0.80) within the lower size classes, but exhibits simultaneously higher amounts of less circular particles for bigger sizes around 100 µm resulting from particle fusion mechanisms. Nevertheless, the amounts of particles in the ranges of lower circularity values are rather neglectable and not affecting further properties or processing. H11 reference powder shows narrower

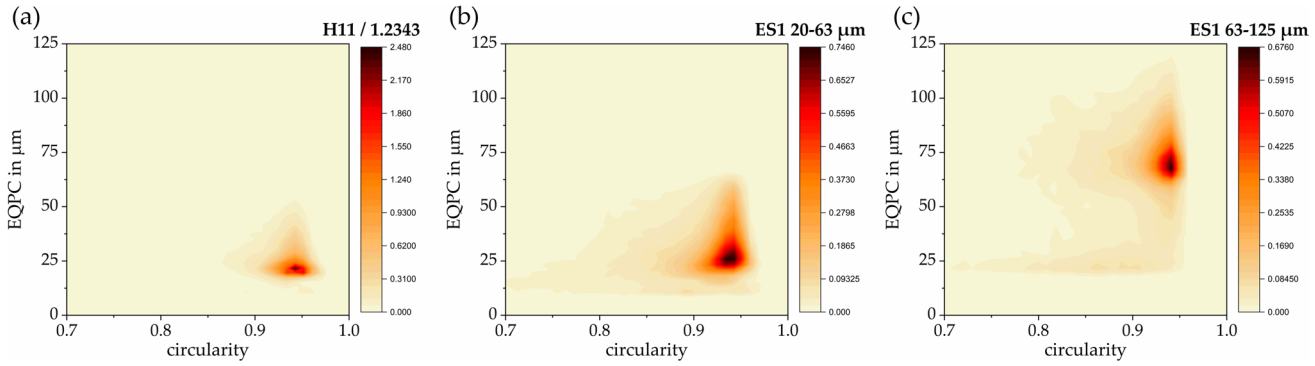

Fig. 4 KDE for H11 (**a**), ES1 20–63 µm (**b**) and 63–125 µm (**c**), EQPC depending on circularity

circularity ranges with a minimum around 0.85, but similar trends could be deduced from the results of EQPC and circularity, where only the amounts of smallest particles differ. When considering particle size-influenced bulk powder properties, this is not disadvantageous (Sect. 3.5). Overall, when focusing on the domains with the highest values of the probability density for circularity values, good results were obtained. For H11, this range is in both dimensions relatively narrow, whereas for the 20–63 µm fraction it scatters more for the circularity values and for 63–125 µm for the EQPC. Furthermore, for the coarser fraction higher amounts of finer particles can be observed, which could be improved by implementing a sifting step. In Supplementary S1 additional KDE are shown regarding the maximum Feret diameter (maximum distance of two parallel tangents at arbitrary angle) and other shape factors (convexity and aspect ratio). Some measuring errors could derive from the non-segmenting of single particles, which are too close to each other, and get counted as a bigger one with significantly lower circularity down to 0.7. For eroded powder fractions this is more often the case compared to H11 because of higher probabilities of particle collision and particle fusion during EDM resulting in slightly lower circularities. Besides that, analyses of projection areas depend strongly on the orientation of possibly not perfectly circular/spherical particles.

3.3 Particle Morphologies

Morphologies of H11 reference (a) and eroded powder fractions 20–63 µm (b) and 63–125 µm (c) are visualized in SEM images in Fig. 5. Most of all, the nearly perfectly circular shape of the eroded particles stands out, which corresponds with the measurements obtained from dynamic image analyses. Compared to the reference powder, not many differences could be found. H11 surfaces seem to be slightly rougher and with micron-sized indentions, which will be examined using atomic force microscopy (AFM) investigations for comparable surface roughness

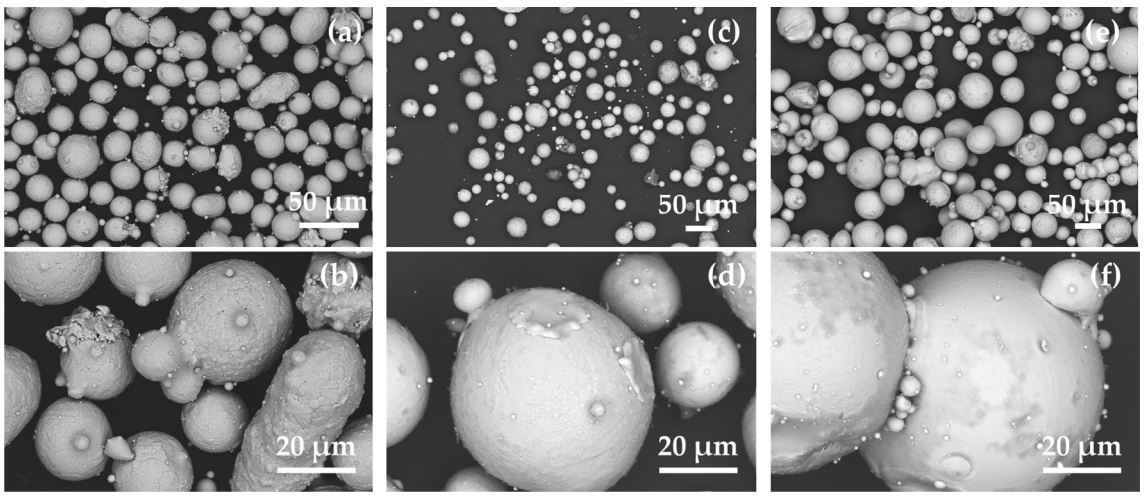

Fig. 5 SEM images of AM reference powder H11 (**a**, **b**); eroded powder fractions ES1 20–63 µm (**c**, **d**) and 63–125 µm (**e**, **f**); two magnifications each (top: 300×, bottom: 1000×)

distributions. Furthermore, the number of satellites seems to be higher. For the smaller fraction some graphite particles and agglomerates around these structures remain, resulting from the graphite electrode due to brittle failure and thermal stresses. The coarser fraction shows nearly no graphitic fragments. In general, the gas atomized H11 seems to develop more defects such as particle fusion, which is indicated by lower circularity values at bigger particle sizes, as seen in the circularity plots (Fig. 3b), compared to eroded powders. For these, this kind of defects are not occurring that much. However, eroded particles show more splats and platelets due to higher particle collision mechanisms in the solidification process and a greater number of agglomerates from sub-micron sized vaporized particles attached to the surface. Overall, the number of defects is at a low level. Moreover, a noticeable amount of surface contaminations could be found. This occurs possibly from the carbon origin in the process itself (tool electrode and dielectric), or possibly from residues of the oil dissolution process after the evaporation of volatile acetone components. An improvement should take place conducting washing steps of filter cakes from filtration experiments via displacement or dilution washing [38]. Processing steps containing water are not recommended due to surface oxidation and possible hydrogen embrittlement in sub-micron sized cracks.

3.4 Chemical Composition and Crystal Structure

3.4.1 ICP OES- and C–S–O-Analyses

Results obtained from the chemical analyses are given in Table 2. As mentioned in Sect. 2.1, EDM-machined components consist of H11/1.2343 martensitic hot work steel and should show its typical alloy composition. In general, the chemical composition corresponds to H11 and could be identified in both fractions. The amount of foreign elements like Cu, Ni or P are in a nominal range or below the detection limit. However, the Si content in H11 and eroded powders is too low compared to data sheets (0.8–1.2 wt%), which is presupposed by the challenges in dissolving Si while boiling in aqua regia. Some marginal residues were observed after filtering the solutions leading to slightly decreased values. A microwave assisted digestion of the powders as well as measurements with X-ray fluorescence spectroscopy (XRF) for quality assurance will help to eliminate this bias.

The biggest difference is observable in the carbon content. Whereas the reference powder shows an expectable C value for steel (hypoeutectoid region) with around 0.4 wt%, the eroded powder fractions have significantly higher values, which differ additionally in each fraction. Their C values amount from 4.4 up to 5 wt%, which is located in the range of cast iron (hypereutectic region) and is accordingly ten times higher. For other steel waste stream sludges, a C-content in this range can be confirmed [29, 30]. The high carbon contents originate from the emerging pyrolysis of the used hydrocarbon-based dielectric fluid [39]. The usage of the graphite electrode alone cannot be the reason, because in [30] metallic tool-shaping electrodes were eroded, meaning in the future it could be focused on alternative dielectrics. It is important to determine, where the carbon is localized within the particle systems. In a former study, some carbon was localized on the particle surfaces, as it could be found with SEM–EDX-analysis [29]. But just this observation alone cannot explain such high carbon amounts. Another factor could be the small amount of remaining graphite particles. To examine the localization of the carbon, XRD measurements were performed and the results are presented in Sect. 3.4.2. Besides the carbon contents, the ratio of oxygen and sulfur is important. The S-content is not differing between the fractions and is on a low level. Similar results are found for O-values, which always amount below 0.1 wt%. For fractions < 20 µm and < 125 µm, respectively, the carbon content differs quite strongly. The smallest fraction shows a C-content of 6.54 wt%, whereas the coarse fraction exhibits a value of 4.73 wt%. For eroded particles < 20 µm an increased oxygen content at 0.21 wt% could be observed.

3.4.2 Carbon Localization via XRD

Figure 6 shows the diffractograms of ES1 20–63 µm and H11. What immediately stands out is the significant difference between both measured patterns, which indicates a transition of the phase composition due to the EDM process. The black pattern (H11) shows typical reflections for a martensitic sample (black squares), i.e., the presence of an adapted body-centered cubic crystal lattice. The remaining reflections are associated to retained austenite (black circles) resulting from the maximum carbon saturation and non-distorting to martensite during the atomization process, namely γ-iron (face-centered cubic). The melting, vaporizing and

Table 2 Composition of eroded powder fractions 20–63 µm and 63–125 µm as well as H11 reference powder obtained from ICP-OES- and C–S–O-analyses

Element/sample	Cr	Cu	Mn	Mo	Ni	P in wt%	Si	V	C	S	O	Fe
ES1 20–63	4.87	0.15	0.35	1.16	0.20	0.010	0.29	0.39	4.98	0.002	0.070	Balance
ES1 63–125	4.95	0.11	0.35	1.17	0.20	0.010	0.22	0.40	4.37	0.002	0.053	Balance
H11/1.2343	5.20	0.02	0.69	1.35	0.08	0.007	0.29	0.39	0.40	0.005	0.031	Balance

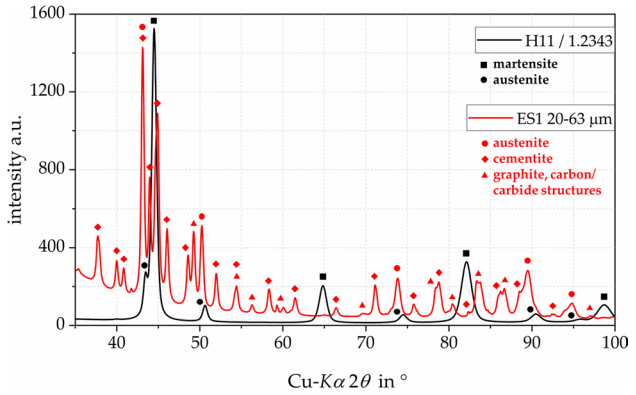

Fig. 6 XRD patterns of H11 reference (black) and eroded particles ES1 20–63 µm (red) for 2θ from 35° to 100° with identified crystal structures of martensite, austenite, cementite and graphite + carbide structures (colored symbols)

rapid solidification during EDM leads to completely different microstructures and a dislocation of the carbon in the iron lattice (red curve).

The sample ES1 20–63 µm shows predominantly cementite (red rhombus), which has an orthorhombic (face centered) crystal lattice instead of martensite. This transition to an orthorhombic lattice implies that carbon atoms are incorporated into the Fe lattice as a result of the high temperature carbon uptake and diffusion mechanisms. It can be stated again that a migration of C-atoms mostly from the pyrolyzed dielectric as well as from the tool electrode takes place, which results in an alloying of the initial material leading to these high C values [35, 40]. Compared to commercial cast iron samples from literature measured with XRD, equivalent reflections were observed in the measurements [41, 42]. Due to the measured C-content (Sect. 3.4.1) and the identification of cementite structures, the assumption that eroded powders feature white cast iron characteristics can be confirmed. Moreover, an increased amount of austenite was identified in the eroded powders compared to the AM powder. The remaining reflections (red triangles) were assigned to mostly hexagonal structures of graphite or formed carbides of alloying elements [43, 44]. In Table 3 the mass fractions for the identified structures are given with their related and adapted lattice parameters. These were obtained from Rietveld refinement as given in Supplementary S2. The entrapped carbon cannot be removed via mechanical processing—hydrometallurgical or thermal processing could be a solution for carbon reduction. Higher carbon contents are rather disadvantageous and challenging when operating with a laser or electron beam, because they can lead to a high evaporation rate and support an unwanted pore formation.

H11 shows 87 wt% martensite and 13 wt% retained austenite, whereas in ES1 20–63 µm no martensite occurs. The refinement of the martensite structure was conducted with a bcc elemental cell because the tetragonal distortion of the crystal lattice in its cell is negligibly small due to the low C-content of 0.4 wt% in the H11 alloy. The austenite in ES1 amounts to approx. 19 wt% and the lattice parameter increases from 0.3598 nm to 0.3629 nm, whereas cementite accumulates to approx. 70 wt% in total. The lattice parameters of the orthorhombic structure are fitting to the values given in the literature [43, 44]. The remaining structures amount to 11 wt% and are summarized in one lattice phase. The fitting of these phases was performed with a hexagonal close-packed structure (hcp), which is represented in this study by graphite. It is assumed, that these graphitic and carbon-based structures include possible remaining surface graphite or agglomerates as well as possible formed carbides of the alloy elements during solidification. For the coarser fraction no major deviations are expected and results from an additional characterization technique are discussed in Sect. 3.6.

3.5 Bulk Powder Properties

Other important requirements besides morphology and chemical composition of the particle systems are the handling and bulk powder properties to ensure an evenly and homogenous powder layer. Therefore, powder density, bulk density, tap density and flow times were measured and are given in Table 4. The material density of reference powder is typically high for Fe-alloys with 7.72 g cm^{-3}. Compared to that, the eroded powder densities remain at comparable values. Due to the transition to cementite and the

Table 3 Identified crystal lattices and their lattice parameters for H11 and ES1 20–63 µm from XRD

Sample/crystal lattice	ES1 20–63 µm	H11/1.2343	Lattice parameter in Å
Martensite (body-centered cubic, bcc)	–	87 wt%	$a = 2.872$
Austenite (face-centered cubic, fcc)	19 wt%	13 wt%	H11: $a = 3.598$ ES1: $a = 3.629$
Cementite (orthorhombic)	70 wt%	–	$a = 5.065$ $b = 6.762$ $c = 4.505$
carbide structures (hexagonal close-packed)	11 wt%	–	$a = 2.496$ $c = 6.735$

Table 4 Densities, tap and bulk densities, Hausner number and flow times of eroded fractions and reference material

sample/value	ES1 < 125 µm	ES1 20–63 µm	ES1 63–125 µm	H11/1.2343 reference
Density in g cm^{-3}	7.54	7.51	7.61	7.72
Bulk density in g cm^{-3}	4.41	4.21	4.19	4.47
Tap density in g cm^{-3}	4.66	4.52	4.45	4.68
Hausner ratio	1.06	1.07	1.06	1.05
Flow time Hall/Carney in s	–	66/15	67/14	72/12

associated different crystal lattice, the density is a bit lower and decreases with higher C-content, as it occurs for the finer eroded fraction. Considering the bulk and tap density, small differences for the sieved fractions occurred. Their values are around 5% less with around 4.20 g cm^{-3} and 4.50 g cm^{-3}, respectively. The initial, with a coarse sieve obtained fraction (< 125 µm) shows similar values as the reference powder with bulk and tap densities of 4.46 g cm^{-3} and 4.65 g cm^{-3}. This difference, compared to both narrower fractions (20–63 µm and 63–125 µm), originates from the fraction of fine and finest particles, which fill the voids between bigger particles. For H11 powder a higher number of satellites could contribute to slightly higher values. Both of these aspects result in advantageous bulk properties. Furthermore, narrower eroded fractions show as fast flow times as the reference material, which indicates their good flowability. Considering the relatively high amount of fine particles for ES1 63–125 µm shown in KDE (Fig. 4c) starting from approx. 20 µm, the comparable result as for the finer fraction may benefit from that. Distinctly lower bulk and tap densities were expected due to coarser particles, but remaining smaller particles fill the voids between the coarser ones increasing these densities. The fraction obtained by sieving with the 125 µm-sieve increased the bulk and tap densities compared to the AM-suited fractions, which profits from included finest particles below 20 µm filling up the smallest voids in the particle collective. A similar trend for H11 could lead to the higher bulk and tap densities due to the higher density in general as well as a PSD slightly shifted to smaller particle sizes (Figs. 3b, 4a) compared to ES1 20–63 µm. One of the most important indicators for bulk solids is the Hausner number which can be calculated by the quotient of tap and bulk powder density. The closer the value to one, the better the flow characteristic of the bulk. Thereby, values between 1.00 and 1.10 represent an "excellent" flow character, whereas values greater than 1.60 are attributed to an "extremely poor" flow character. All four measured powders exhibit an excellent flow behavior with values between 1.05 (H11) and 1.07 (ES1 20–63 µm), which was assumed after the first simple handling tests and the good results obtained from dynamic image analysis, as the particle shape (circularity) correlates directly with bulk powder mechanics and flowability characteristics. Overall, eroded powder fractions fulfill the requirements for handling properties well and are fully comparable with reference materials. An uniformly and evenly distributed powder layer will be ensured while applying these powders with a squeegee tool.

3.6 Microstructure Analysis of Eroded Particles

3.6.1 Powder Metallography

The microstructure of the eroded powders is presented in the micrographs in Fig. 7, whereas the finer fraction is shown at the top (a + b) and the coarser fraction at the bottom (c + d). In all images, the 2D cross sections show nicely circular shaped particles with a low number of defects—particle fusion just occurs in two cases and some minor dents at the outer shells—and nearly no satellites. Within both fractions, no significant differences can be seen. However, in Fig. 7c at the right edge, one single hollow particle (approx. 70 µm) was revealed after grinding. In this bigger hollow one, two other single particles are entrapped, possibly due to some gradients during resolidification, collapsing of the generated cavitation bubble or gas bubble explosions during the EDM mechanism [45], after the frequent disabling of the electrical potential and current flow. In general, all the particles look relatively homogenous. The outer areas show a needle- or plate like-corona, which could be attributed to primary solidified cementite, whereas the inner sections appear differently caused by etchability differences due to varying chemical concentrations of the elements. The fineness of the microstructure as well as their type of constituents has to be taken into account. What is striking within all particles is a clear over- or under-etching of the cross-sections. Due to chemical gradients within each single particle the etched surfaces and obtained contrasts for the microstructures can differ quite strongly, resulting from minor differences in their micro-chemistry, which could be seen in SEM–EDX measurements of single particles. As ICP OES gives results for the chemical composition of the bulk, these deviations cannot be detected. The variation of chemical composition results from the rapid cooling as well. Due to very high temperature gradients and high collision rates the probability of randomly distributed

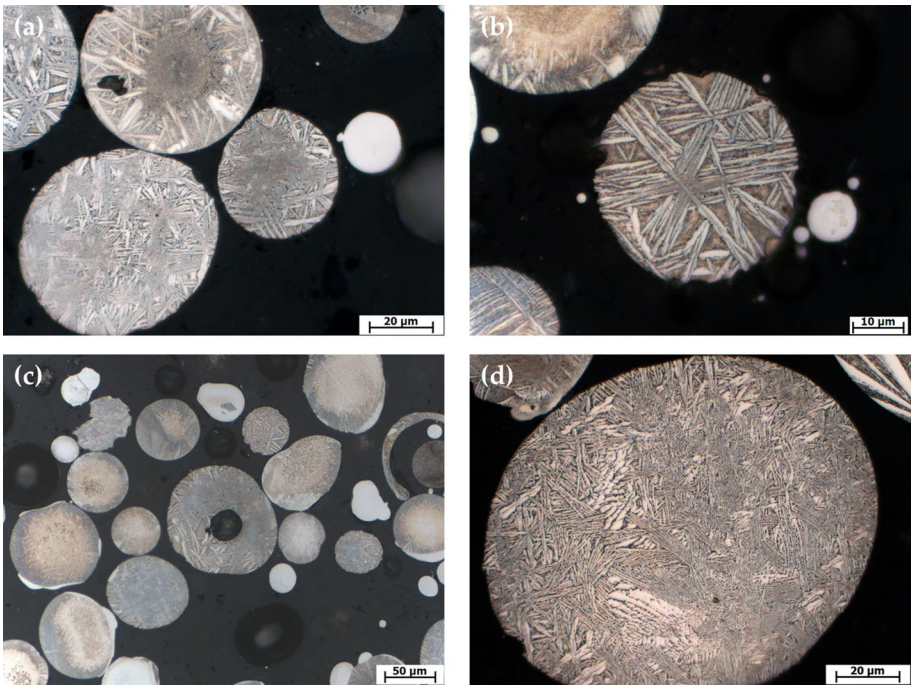

Fig. 7 Light microscopy cross sections of embedded, ground, polished and etched powder samples of ES1 20–63 µm (**a**, **b**) and ES1 63- 125 µm (**c**, **d**); magnifications: (**a**) and (**d**) 1000×, (**b**) 1600×, (**c**) 320×

molten and vaporized areas with differing compositions and diffusion-controlled segregation leads to inhomogeneous solidification rates and particles with slightly changing alloying ranges.

The high C-contents of approx. 4.4 wt% and 5.0 wt% revealed the presence of a white cast iron-like material. In these, a ledeburitic microstructure is characteristic in most cases [46]. However, in the obtained micrographs no structures of ledeburitic origin can be found. The observed microstructure consists of austenite and cementite, being acicular primary solidified cementite resulting from abrupt and extreme undercooling of the melt [46], which fits to the high temperature gradients and rapid solidification of eroded material in EDM. The remaining surrounding structures could be attributed to retained austenite developed in the further process of solidification. It can be assumed that in the case of rapid solidification away from equilibrium, acicular cementite initially forms from the melt and the residual melt solidifies austenitic. Due to the high cooling rates of the particles, a transformation of the remaining austenite into, e.g., pearlite is suppressed. In case of an atomization of a white cast iron melt in nitrogen atmosphere, Gulyaev et al. reported the development of primary cementite in the hypereutectic range [47]. This would coincide with the findings from XRD measurements indicating cementite as well as austenite structures. Besides that, no other bibliography could be found reporting about this developed microstructure.

3.6.2 Identification of Microstructural Phases

However, to proof these assumptions in a second instance, SEM-EBSD investigations were examined on particles of the coarser fraction ES1 63–125 µm. Measurements were carried out on structures of the inner regions, whose representative result is illustrated in Fig. 8, as well as in the outer regions of the particles. The phases cementite and austenite are clearly identified by their different crystal structures. The presence of the assumed microstructure could be proven. Cementite phases amount to 74 vol%, which correlates quite well with the XRD results of 70 wt%, whereas austenite phases show a higher value with 26 vol% compared to the 19 wt% in XRD. The differences may originate in the analyzing techniques themselves, because powder XRD measures bulk properties, whereas in EBSD significantly smaller areas—in our case inner and outer particle regions—were investigated. Moreover, the XRD measurement contains additionally a certain amount of graphite due to possible processing residues, while in EBSD no hcp structures were detected. Major differences regarding the phase shares between the inner and outer regions have not been found with results of maximum 78 vol% of cementite and 22 vol% of austenite. The high carbon contents of approx. 4.4 wt% to 5.0 wt%, the revealed microstructures in the micrographs and the EBSD results leading to the final conclusion that the eroded particles feature acicular primary cementite and retained austenite.

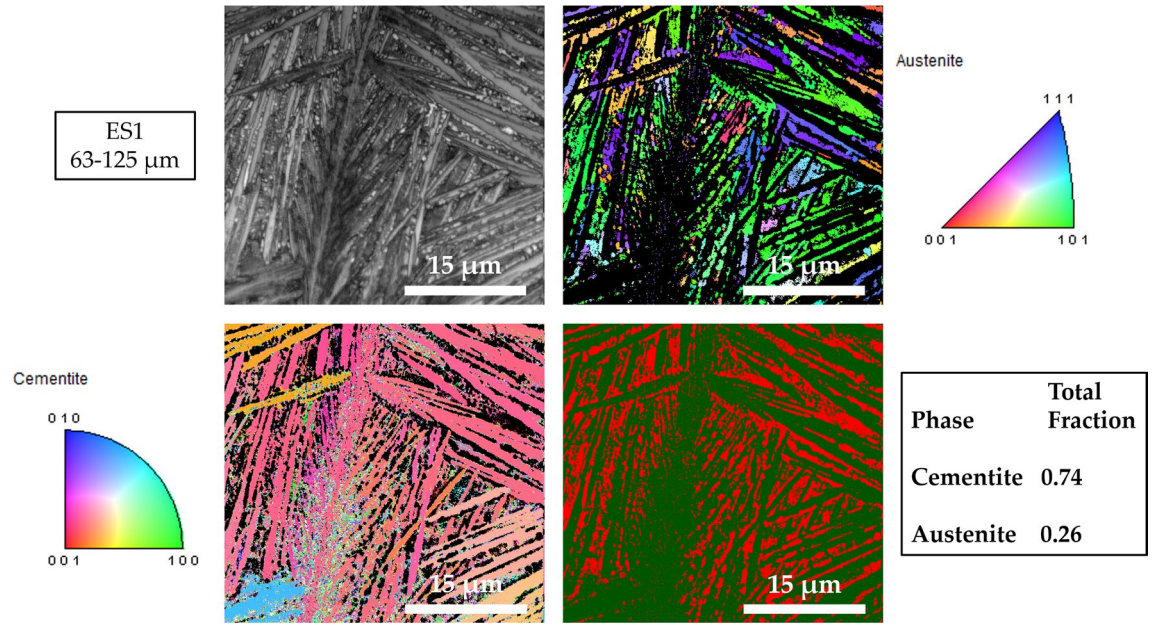

Fig. 8 EBSD-imaging of ES1 63–125 µm for identifying the microstructure and determining the total fraction of austenite (red) and cementite (green)

3.7 Developed Microstructure and Internal Structure After Remelting

As the eroded powders should be processed in several AM-techniques, it is important to know how the particle collective behaves during heating, melting and resolidifying under certain conditions. The developed microstructure is of interest as it predominantly influences the final part properties and has to be examined in a light microscope. Besides that, the inner structure and detection of porous areas or other imperfections within a solid specimen has to be studied. Therefore, the underneath stated results should help to figure out the resulting structural properties of a solid sample. The melting and formation of a solid sample of non-fractionated powder ES1 < 125 µm was determined in a TGA–DSC device. During the experiment a total weight loss of 1.03 wt% could be observed up to 1500 °C. No anomalous behavior in the DSC curve could be observed, as the powder behaves like cast iron. Simultaneously coupled FTIR measurements showed no CH–, CH_2– or CH_3-stretching and bending vibrations, which are typical for the organic hydrocarbon-based dielectrics [48]. Furthermore, sharp and intense peaks of carbon dioxide bands could be detected [49] indicating a release of an uncertain amount of carbon at higher temperatures. In Supplementary S3 three FTIR spectra are presented for the hydrocarbon-based dielectric and for occurring CO_2 peaks at two different temperatures, whereas the CO_2 peaks are observable during wide ranges of the heating.

To investigate the microstructure and inner structure of materials with a non-destructive method, the application field of X-ray micro-computed tomography (µ-CT) was extended to materials characterization and particle technology [50, 51], as it reveals new insights into the understanding of different processes and property relationships. The arrangements of the X-ray and suitable scanning settings is important for a good result regarding resolution, sample shift, beam hardening, ring artifacts, noise and other measurement artefacts [52]. In µ-CT, the information is based on different attenuations and interactions of X-ray photons with the matter following the Beer-Lambert's law. Thereby, different phases and structures are revealed due to the materials density difference. After measurements, segmentation is performed after post-processing of the reconstructed data and image stacks. Each phase of the sample gets assigned to a specific grey value and is analyzed quantitatively regarding different properties. In the context of AM, µ-CT investigations are useful for examining produced powders and detecting possible hollow structures or particles within the powder bulk [53]. Secondly, a revealing of the inner structure and the quantification of porosities in printed specimen is important because the presence of voids, precipitations, segregations or other imperfections affect the material performance negatively leading to internal defects, areas for crack initiation or premature fatigue failure [54].

3.7.1 Microstructure Analysis

In Fig. 9 the evolved microstructure of the compact sample after TGA with undefined oven cooling is presented. Overall, a significant change in the appearing phases can be seen. A ledeburitic microstructure (mainly ledeburite II) was observed at room temperature, as it is typical for white cast iron materials [41, 46]. From the light micrographs, a microstructure is evident that typically forms in a hypoeutectic iron alloy with less than 4.3 wt% C. However, from C-analyses of the initial powder samples a carbon content of approx. 4.7 wt% was measured. It is a crucial point meaning that the compact samples should exhibit a hypereutectic microstructure containing acicular primary cementite, which cannot be found. This indicates a carbon loss correlating with strong CO_2 peaks in vapor-FTIR during heating. It can be attributed to a possible slight decarburization process in the molten or pre-molten state [55]. The microstructure is characterized by brownish pearlitic areas (brown arrows in Fig. 9) and cementite marked by green arrows. The pearlite was formed from primary austenite during furnace cooling in the TGA cell. In addition, retained austenite (orange arrows) was found in ledeburite II. This can be explained with contained alloying elements, especially the higher amount of chromium, which is suppressing a pearlite formation during cooling. Depending on the stability of the retained austenite, some of this may transform to martensite during cooling to room temperature. Due to the high carbon concentration, plate martensite was observed in retained austenite islets, which is marked with dark blue arrows in Fig. 9. Due to the ledeburitic microstructure, poor machinability, high hardness and brittle material behavior can be assumed [56]. Further characterization of the mechanical properties, especially the (micro)hardness and tensile strength of generated specimen or layers of out eroded particles, can provide further insights in a future work.

3.7.2 Analysis of Inner Structure and Defects

For examining the inner structure and evaluating the internal porosity of the compact sample gained from TGA investigations in a µ-CT device were carried out. In Fig. 10 the reconstruction of the overview scan (a) and the high-resolution scan including the highlighted pores separated from the matrix (b) are visualized. In the overview scan in Fig. 10a a rough and very jagged surface can be observed. The slight density difference between austenite ($\rho = 7.87$ g cm^{-3}) and cementite ($\rho = 7.69$ g cm^{-3}) can be recognized in Fig. 10b with brighter greyscale representing higher dense phases and darker greyscale representing lower dense phases. Thus, retained austenite is visible as bright grey and cementite as darker grey in the µ-CT scan. However, as already shown in the cross-sectional image slices of Sect. 2.3.7, pores were detected within the sample. The segmented and labeled pores (colored) are shown in the front of Fig. 10b. It can be clearly seen, that the pores differ strongly in their sizes and shapes and their type of open and closed ones. Porous areas may originate from the lack of fusion between particles due to the presence of adjacent melt pools or entrapped gas bubbles. Furthermore, in this sample the melting takes place over a very broad range of particles up to 125 µm, which may lead to pores due to a non-filling of open volume. The particles do not have exactly the same melting and solidifying temperatures which could lead to pre-solidified areas resulting in the observed pores and voids. That is caused by their difference in the micro-chemistry, which was already seen in the different etchabilities (Sect. 3.6.1). Moreover, at the walls of the crucible a beneficiary pore formation is observed due to heat dissipation influencing negatively the cooling and solidification process. Therefore, improvements in the cooling regime as well as in the cooling setup are recommended.

With the help of analyses tools in ORS DragonFly software the size, volume and shape of the pores were determined with a total number of 1305 segmented pores. The volume of the pores totals to approx. 9.5 mm^3, which results

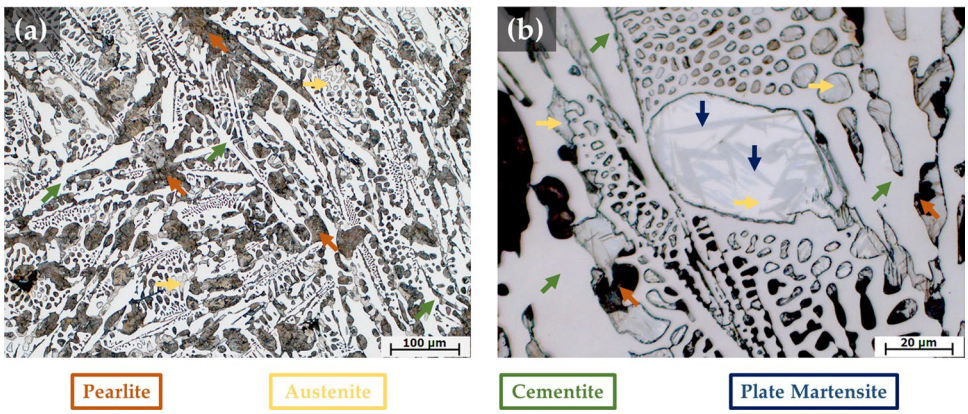

Fig. 9 Light microscopy images of embedded, ground, polished and etched TGA–DSC sample ES1 < 125 µm after melting and solidifying in a alumina crucible; with assignments of occurring microstructure by colored arrows belonging to underneath listed and identified pearlite, austenite, cementite and plate martensite; magnifications: (**a**) 200 × and (**b**) 1000 ×

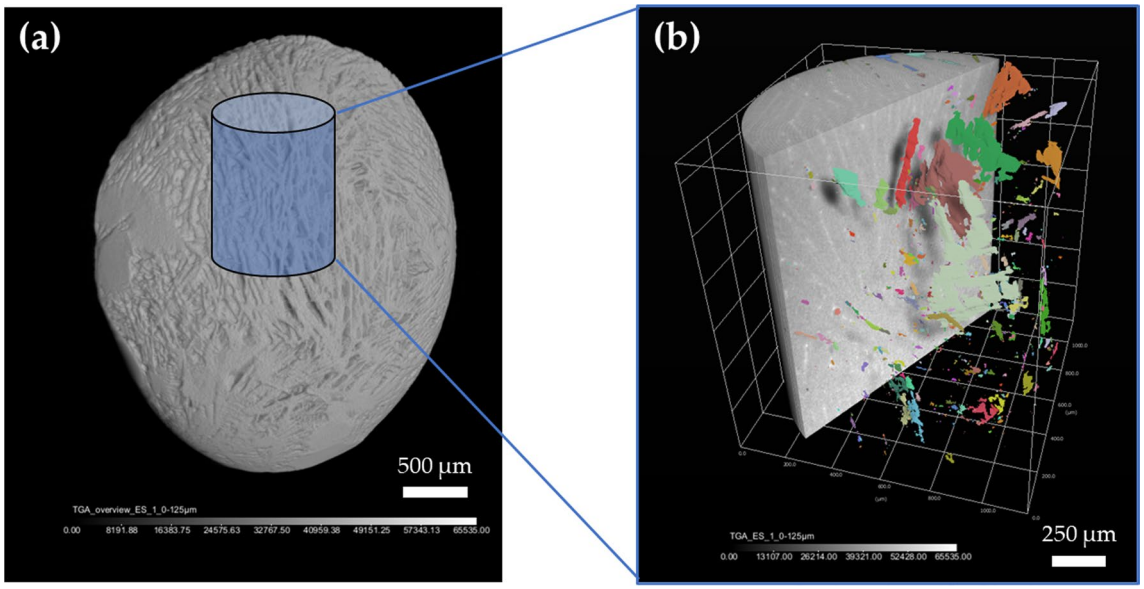

Fig. 10 µ-CT scan of compact TGA–DSC sample ES1 < 125 µm; (**a**) 3D-visualization of overview scan with cylindrical shaped cut-out; (**b**) 3D-visualization of high-resolution scan after deep learning algorithm with highlighted pores (back as compact sample; front without matrix from filtering showing pore volume)

in a porosity value of the investigated volume (approx. 1327 mm^3) of 0.72%. These pores could be points of crack initiation or can support a crack propagation leading to a premature material fatigue and failure. Compared to other particle systems and manufacturing techniques as in AM, casting processes, sintering or hot isostatic pressing, where different constraints are present, this achieved porosity value cannot be seen as too bad. On the one hand, for specimen printed via SLM or EBM porosity values of max. 0.5% are common [54], which cannot be completely reached with eroded powders in this simple experiment. Compared to smaller printed parts in SLM of reused metal powders, Giganto et al. reports a higher porosity with approx. 1.0% to 1.2% [57]. Specimen produced in BJT-techniques, on the other hand, show significantly higher values for porosity of approx. up to 10% [15]. For castings it is complicated to give exact porosity values, as several different pore origin, pore nucleation and pore growth mechanisms are present [58]. However, observable pores are significantly bigger and reach values over 2% and even clearly higher porosities [59]. In Fig. 11 the Feret diameters, pore volume and their aspect ratio are presented. The $x_{50,0}$ value of the $Feret_{mean}$ pore diameter amounts to 8.4 µm, whereas the pore volume shows a median of 140 $µm^3$. These pores are completely indifferently and irregularly shaped, which can be stated in the broader pore aspect ratio distribution with a median value of 0.4. In conclusion, it remains to be noted that the porosity needs to be decreased by improving the cooling regime, implementing a stationary section and defined cooling rates to control the undercooling of the melt and the microstructure development, respectively.

4 Conclusion

In this study, a holistic characterization of eroded particles extracted from waste sludges originating from EDM was performed in order to reuse them as recycled powders for AM processes. The particle size and shape distributions of sieved eroded powder fractions and a commercial reference material as well as their chemical composition, crystal structure and bulk powder properties were investigated. Further metallographic investigations of the microstructure of eroded powders and obtained compact samples from thermal analysis as well as µ-CT measurements were conducted for obtaining information about the inner structure and occurring defects. The major findings are summarized in the following key points:

- Waste streams from filter cartridges are not suitable in a recycling process for extracting metallic particles due to low yields, time consuming dismantling steps and high amounts of too small particles. In contrast, the recycling of sludges from the basin is promising.
- Eroded particles fulfill the AM-requirements regarding particle size, particle shape, allowable number of geometric defects as well as powder flowability characteristics. All these properties are fully comparable to the considered AM reference material.
- The chemical composition of eroded powder fractions is comparable to the machined alloy and low concentrations of foreign elements were detected. However, the C-contents are very high resulting from a pyrolysis of

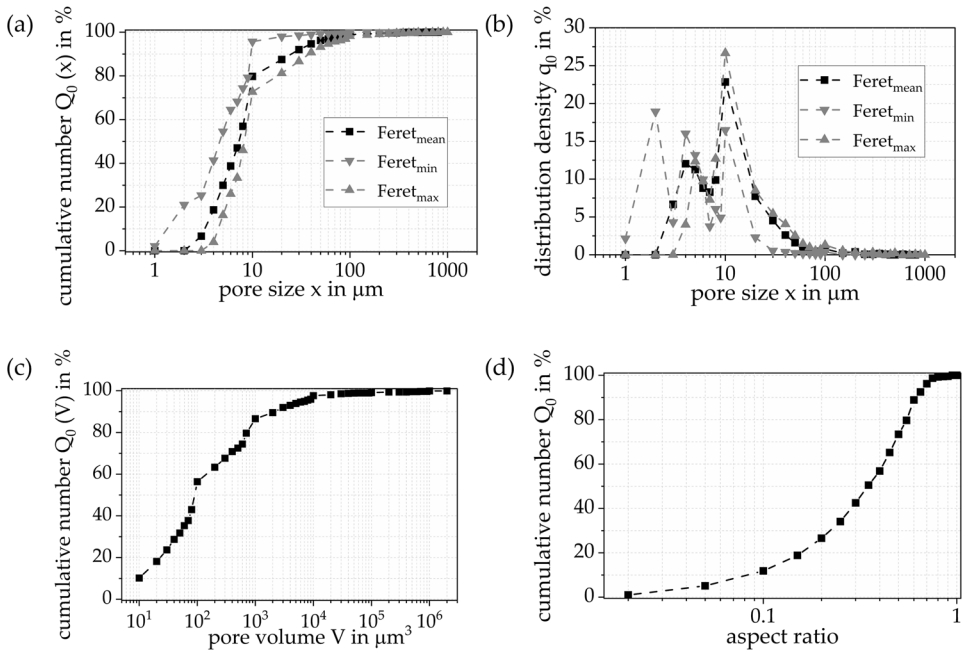

Fig. 11 Pore distributions obtained from DragonFly data; (**a**) pore size distribution Q0; (**b**) pore distribution density q0 (both in terms of three Feret diameters); (**c**) pore volume distribution Q0; (**d**) aspect ratio distribution Q0 of pores

the dielectric. The element C is dissolved in the Fe lattice and leads to a hypereutectic composition. Due to the high temperature gradient during rapid solidification, primary cementite formed in the powder particles.

- For all samples, the eroded powders have a microstructure of austenite and primary cementite and almost no hollow bodies or porosity, as shown in the 2D data of the micrographs. A compact sample of eroded powder showed a change in microstructure to ledeburite II and pearlite. Some retained austenite with embedded plate martensite was found in the ledeburitic structure.
- Micro-CT investigations provided 3D information of the inner structure of a compact sample. A pore formation was observed with strongly differing sizes and shapes presented in pore distributions.

Concerning the applicability of recycled eroded particles in industrial fields can be supported by these findings. Successful pre-tests in laser beam direct energy deposition (laser cladding; laser welding; LB-DED) were performed resulting in layers without cracks. Several powder mixtures with commercially available materials are still leading to a reduction of costs and energy consumption regarding the raw material supply. This approach of powder mixtures can be transferred to BJT in its most commonly infiltration and sintering pathways by using a wide range of particle sizes. Certainly, recycled fractions and their behavior as well as resulting properties of manufactured parts via SLM and EBM devices have to be studied. Adapting these investigations with powder mixtures again should help to reduce the energy and costs of the primary raw powder production. Another application field for components out of the recycled powders and a cost reduction can be seen in powder metallurgy in general. More precisely, a production of specimen in spark plasma sintering (SPS) or field assisted sintering techniques (FAST) should be aimed for and tested. Lastly, a possible usage of recycled powders for generating support structures in AM of non-metallic components or composite materials can be taken into account. Other future tasks should deal with a C-reduction as well as investigations of several cooling regimes and different cooling rates for the recycled fractions and their dependence on the microstructure development. These temperature profiles can be combined with a stationary regime after reaching the molten state for different dwell times to induce decarburization processes of the samples. Another approach for decreasing the C-content could be the processing of eroded powders in a rotating pyrolysis furnace.

Supplementary Information The online version contains supplementary material available at https://doi.org/10.1007/s12540-023-01574-9.

Acknowledgements The authors would like to thank the technicians Annett Kästner, Yvonne Volkmer and Elvira Kleen of MVTAT institute for conducting granulometric analysis, bulk powder investigations and ICP OES measurements. In addition, the authors thank Gert Schmidt (TUBAF, IKFVW) for taking SEM images, Thilo Kreschel for measuring samples in C–S–O-analyzers and Janet Kreschel (both TUBAF, IEST) for preparing metallographic investigations.

Author Contributions Conceptualization: OV; Methodology: OV, MW, AS; Validation: OV; Formal analysis: OV; AS; Investigation: OV, MW, AS, HS, CQ; Data curation: OV; Writing—original draft preparation: OV; Writing—review and editing: MW, AS; HS, CQ, UAP; Visualization: OV, MW, AS; Supervision: UAP; Project administration: OV,

UAP; Funding acquisition: UAP. All authors have read and agreed to the published version of the manuscript.

Funding Open Access funding enabled and organized by Projekt DEAL. The authors thank the funding for their research as part of the IGF project 21692 BR "Erhöhung der Rohstoffeffizienz durch Nutzung von Reststoffströmen aus dem Senkerodieren für Prozesse der Additiven Fertigung" (Increasing raw material efficiency by using waste streams from die-sink electro discharge machining for additive manufacturing). This project is supported via the German Federation of Industrial Research Associations (AiF) within the program for promoting the Industrial Collective Research (IGF) funded by the German Federal Ministry for Economic Affairs and Climate Action (BMWK), based on a resolution of the German Parliament (Bundestag).

Declarations

Conflicts of interest The authors declare no conflict of interest. The authors declare they have no financial interests.

References

1. K.H. Ho, S.T. Newman, State of the art electrical discharge machining (EDM). Int. J. Mach. Tools Manuf **43**(13), 1287–1300 (2003). https://doi.org/10.1016/s0890-6955(03)00162-7
2. B.M. Schumacher, After 60 years of EDM the discharge process remains still disputed. J. Mater. Process. Technol. **149**(1–3), 376–381 (2004). https://doi.org/10.1016/j.jmatprotec.2003.11.060
3. L. Li, Z.Y. Li, X.T. Wei, X. Cheng, Machining characteristics of Inconel 718 by sinking-EDM and wire-EDM. Mater. Manuf. Process. **30**(8), 968–973 (2014). https://doi.org/10.1080/10426914.2014.973579
4. F.N. Leão, I.R. Pashby, A review on the use of environmentally-friendly dielectric fluids in electrical discharge machining. J. Mater. Process. Technol. **149**(1–3), 341–346 (2004). https://doi.org/10.1016/j.jmatprotec.2003.10.043
5. C.R. Sanghani, G.D. Acharya, Effect of various dielectric fluids on performance of EDM: a review. Trends Mech. Eng. Techol. **6**(1), 55–71 (2016)
6. T. DebRoy, H.L. Wei, J.S. Zuback, T. Mukherjee, J.W. Elmer, J.O. Milewski, A.M. Beese, A. Wilson-Heid, A. De, W. Zhang, Additive manufacturing of metallic components—process, structure and properties. Prog. Mater. Sci. **92**, 112–224 (2018). https://doi.org/10.1016/j.pmatsci.2017.10.001
7. T.D. Ngo, A. Kashani, G. Imbalzano, K.T.Q. Nguyen, D. Hui, Additive manufacturing (3D printing): a review of materials, methods, applications and challenges. Compos. B Eng. **143**, 172–196 (2018). https://doi.org/10.1016/j.compositesb.2018.02.012
8. A. Strondl, O. Lyckfeldt, H. Brodin, U. Ackelid, Characterization and control of powder properties for additive manufacturing. JOM **67**(3), 549–554 (2015). https://doi.org/10.1007/s11837-015-1304-0
9. J.P. Kruth, L. Froyen, J. Van Vaerenbergh, P. Mercelis, M. Rombouts, B. Lauwers, Selective laser melting of iron-based powder. J. Mater. Process. Technol. **149**(1–3), 616–622 (2004). https://doi.org/10.1016/j.jmatprotec.2003.11.051
10. M. Munsch, M. Schmidt-Lehr, E. Wycisk, *Metal Additive Manufacturing with Sinter-Based Technologies* (AM Power Insights, Hamburg,, 2018). https://ampower.eu/insights/additive-manufacturing-sinter-based-technologies/
11. C.Y. Yap, C.K. Chua, Z.L. Dong, Z.H. Liu, D.Q. Zhang, L.E. Loh, S.L. Sing, Review of selective laser melting: materials and applications. Appl. Phys. Rev. **2**, 041101 (2015). https://doi.org/10.1063/1.4935926
12. L.E. Murr, S.M. Gaytan, D.A. Ramirez, E. Martinez, J. Hernandez, K.N. Amato, P.W. Shindo, F.R. Medina, R.B. Wicker, Metal fabrication by additive manufacturing using laser and electron beam melting technologies. J. Mater. Sci. Technol. **28**(1), 1–14 (2012). https://doi.org/10.1016/s1005-0302(12)60016-4
13. C. Körner, Additive manufacturing of metallic components by selective electron beam melting—a review. Int. Mater. Rev. **61**(5), 361–377 (2016). https://doi.org/10.1080/09506608.2016.1176289
14. A. Mostafaei, A.M. Elliott, J.E. Barnes, F. Li, W. Tan, C.L. Cramer, P. Nandwana, M. Chmielus, Binder jet 3D printing—process parameters, materials, properties, modeling, and challenges. Progress Mater. Sci. **119**, 100707 (2021). https://doi.org/10.1016/j.pmatsci.2020.100707
15. Y. Bai, G. Wagner, C.B. Williams, Effect of particle size distribution on powder packing and sintering in binder jetting additive manufacturing of metals. J. Manuf. Sci. Eng. **139**, 8 (2017). https://doi.org/10.1115/1.4036640
16. R.V. Mendagaliev, D.D. Evdokimov, A.M. Firsov, A.M. Vildanov, A.D. Evstifeev, V.I. Maksimochkin, R.A. Grachev, O.N. Dubinin, S.A. Evlashin, O.G. Klimova-Korsmik, Direct laser deposition of austenitic and martensitic steel gradient layers. Met. Mater. Int. **29**(5), 1555–1562 (2023). https://doi.org/10.1007/s12540-022-01306-5
17. W. Choo, M. Ebrahimian, K. Choi, J.H. Kim, Influence of heat treatment on the microstructure and hardness of 17-4PH stainless steel fabricated through direct energy deposition. Met. Mater. Int. **29**(6), 1750–1760 (2023). https://doi.org/10.1007/s12540-022-01333-2
18. I. Gibson, D. Rosen, B. Stucker, M. Khorasani, *Additive Manufacturing Technologies*, 3rd edn. (Springer, Cham, 2021), p.685
19. S. Vock, B. Klöden, A. Kirchner, T. Weißgärber, B. Kieback, Powders for powder bed fusion: a review. Progress Addit. Manuf. **4**(4), 383–397 (2019). https://doi.org/10.1007/s40964-019-00078-6
20. Y. Tsunekawa, T. Ueno, M. Okumiya, T. Yashiro, Plasma sprayed coatings with water and gas atomised bearing steel powders. Surf. Eng. **19**(1), 17–22 (2013). https://doi.org/10.1179/026708402225010074
21. D. Beckers, N. Ellendt, U. Fritsching, V. Uhlenwinkel, Impact of process flow conditions on particle morphology in metal powder production via gas atomization. Adv. Powder Technol. **31**(1), 300–311 (2020). https://doi.org/10.1016/j.apt.2019.10.022
22. Statistisches Bundesamt. *Kleine und mittlere Unternehmen*. 2020. Available from: https://www.destatis.de/DE/Themen/Branchen-Unternehmen/Unternehmen/Kleine-Unternehmen-Mittlere-Unternehmen/_inhalt.html
23. G. Soundarapandiyan, C. Johnston, R.H.U. Khan, B. Chen, M.E. Fitzpatrick, A technical review of the challenges of powder recycling in the laser powder bed fusion additive manufacturing

process. J. Eng. **2021**(2), 97–103 (2021). https://doi.org/10.1049/tje2.12013
24. C. Lu, R. Zhang, M. Xiao, X. Wei, Y. Yin, Y. Qu, H. Li, P. Liu, X. Qiu, T. Guo, A comprehensive characterization of virgin and recycled 316L powders during laser powder bed fusion. J. Market. Res. **18**, 2292–2309 (2022). https://doi.org/10.1016/j.jmrt.2022.03.125
25. O. Rayan, J. Brousseau, C. Belzile, A. El Ouafi, Maraging steel powder recycling effect on the tensile and fatigue behavior of parts produced through the laser powder bed fusion (L-PBF) process. Int. J. Adv. Manuf. Technol. **127**(3-4), 1737–1754 (2023). https://doi.org/10.1007/s00170-023-11522-x
26. V.V. Popov Jr., A. Katz-Demyanetz, A. Garkun, M. Bamberger, The effect of powder recycling on the mechanical properties and microstructure of electron beam melted Ti-6Al-4V specimens. Addit. Manuf. **22**, 834–843 (2018). https://doi.org/10.1016/j.addma.2018.06.003
27. H.P. Tang, M. Qian, N. Liu, X.Z. Zhang, G.Y. Yang, J. Wang, Effect of powder reuse times on additive manufacturing of Ti-6Al-4V by selective electron beam melting. JOM **67**(3), 555–563 (2015). https://doi.org/10.1007/s11837-015-1300-4
28. J. Richter, T. Wegener, R. Kratzsch, M. Vollmer, U. Peuker, T. Niendorf, On the structural integrity and fatigue performance of additively manufactured Ti-6Al-4V parts processed using mechanically recycled powders. Int. J. Fatigue **176**, (2023). https://doi.org/10.1016/j.ijfatigue.2023.107903
29. O. Voigt, U.A. Peuker, Suitability of eroded particles from Die-Sink electro discharge machining for additive manufacturing—review. Charact. Process. Metals **12**(9), 1447 (2022). https://doi.org/10.3390/met12091447
30. K. Oßwald, J. Woidasky, A.M. Hoffmann, M. Moser, Suitability of electrical discharge machining debris particles for usage as a powder for selective laser melting: an explorative study. Prog. Addit. Manuf. **4**(4), 443–449 (2019). https://doi.org/10.1007/s40964-019-00080-y
31. M. Dvornik, E. Mikhailenko, Preparation of powder by electrical discharge erosion and sintering of ultrafine WC-5TiC-10Co alloy with high hardness. Int. J. Refract. Met. Hard Mater. **112**, (2023). https://doi.org/10.1016/j.ijrmhm.2023.106154
32. F. Huber, C. Bischof, O. Hentschel, J. Heberle, J. Zettl, K.Yu. Nagulin, M. Schmidt, Laser beam melting and heat-treatment of 12343 (AISI H11) tool steel—microstructure and mechanical properties. Mater. Sci. Eng. A **742**, 109–115 (2019). https://doi.org/10.1016/j.msea.2018.11.001
33. G. Deng, L. Cahill, An adaptive Gaussian filter for noise reduction and edge detection, *in 1993 IEEE Conference Record Nuclear Science Symposium and Medical Imaging Conference*, vol. 3 ((IEEE, 1993), pp. 1615–1619. https://doi.org/10.1109/NSSMIC.1993.373563
34. O. Ronneberger, P. Fischer, T. Brox. U-net: Convolutional Networks for Biomedical Image Segmentation, in Medical Image Computing and Computer-Assisted Intervention–MICCAI 2015, ed. by N. Navab, J. Hornegger, W.M. Wells, A.F. Frangi. 18th International Conference on Medical Image Computing and Computer Assisted Intervention, Munich, 5–9 October 2015, Part III. Lecture Notes in Computer Science, vol. 9351 (Springer, 2015). https://doi.org/10.1007/978-3-319-24574-4_28.
35. J.S. Soni, Microanalysis of debris formed during rotary EDM of titanum alloy (Ti6Al4V) and die steel (T215Cr12). Wear **177**, 71–79 (1994). https://doi.org/10.1016/0043-1648(94)90119-8
36. A.K. Khanra, L.C. Pathak, M.M. Godkhindi, Microanalysis of debris formed during electrical discharge machining (EDM). J. Mater. Sci. **42**(3), 872–877 (2007). https://doi.org/10.1007/s10853-006-0020-0
37. S. Węglarczyk, Kernel density estimation and its application. ITM Web Conf.**23**(2), 00037 (2018). https://doi.org/10.1051/itmconf/20182300037
38. M. Wilkens, U.A. Peuker, Grundlagen und aktuelle Entwicklungen der Filterkuchenwaschung—fundamentals and recent developments in filter cake washing. Chem. Ing. Technol. **84**(11), 1873–1884 (2012). https://doi.org/10.1002/cite.201200095
39. A.E. Berkowitz, J.L. Walter, Spark erosion: a method for producing rapidly quenched fine powders. J. Mater. Res. **2**(2), 277–288 (1987). https://doi.org/10.1557/JMR.1987.0277
40. A.S. Gill, S. Kumar, Surface alloying of H11 die steel by tungsten using EDM process. Int. J. Adv. Manuf. Technol. **78**(9–12), 1585–1593 (2015). https://doi.org/10.1007/s00170-014-6743-1
41. L. Battezzati, P. Baldi, M. Baricco, E. Bosco, C.A. Goria, G. Serramoglia, F. Marongiu, Solidification experiments for the study of phase selection in cast iron. Int. J. Cast Met. Res. **16**(1–3), 125–129 (2003). https://doi.org/10.1080/13640461.2003.11819570
42. J. Chakraborty, M. Ghosh, R. Ranjan, G. Das, D. Das, S. Chandra, X-ray diffraction and Mössbauer spectroscopy studies of cementite dissolution in cold-drawn pearlitic steel. Philos. Mag. **93**(36), 4598–4616 (2013). https://doi.org/10.1080/14786435.2013.838010
43. M.R. Shabgard, F. Kabirinia, Effect of dielectric liquid on characteristics of WC-Co powder synthesized using EDM process. Mater. Manuf. Process. **29**(10), 1269–1276 (2014). https://doi.org/10.1080/10426914.2013.852207
44. J.E. Bridge, G.N. Maniar, T.V. Philip, Carbides in M-50 high speed steel. Metall. Trans. **2**, 2209–2214 (1971). https://doi.org/10.1007/BF02917552
45. W. König, F. Klocke, *Fertigungsverfahren: Abtragen, Gnerieren und Lasermaterialbearbeitung*, vol. 4 (Springer, Auflage, 2007), p.412
46. J. Campbell, A hypothesis for cast iron microstructures. Metall. Mater. Trans. B **40**, 786–801 (2009). https://doi.org/10.1007/s11663-009-9289-0
47. A.P. Gulyaev, S.I. Astakhov, Structural features of atomized white cast iron powder. Met. Sci. Heat Treat. **33**(1), 56–60 (1991). https://doi.org/10.1007/BF00775038
48. A.B.D. Nandiyanto, R. Oktiani, R. Ragadhita, How to read and interpret FTIR spectroscope of organic material. Indones. J. Sci. Technol. **4**(1), 97–118 (2019). https://doi.org/10.17509/ijost.v4i1.15806
49. V. Tucureanu, A. Matei, A.M. Avram, FTIR spectroscopy for carbon family study. Crit. Rev. Anal. Chem. **46**(6), 502–520 (2016). https://doi.org/10.1080/10408347.2016.1157013
50. V. Cnudde, M.N. Boone, High-resolution X-ray computed tomography in geosciences: a review of the current technology and applications. Earth Sci. Rev. **123**, 1–17 (2013). https://doi.org/10.1016/j.earscirev.2013.04.003
51. T. Leißner, A. Diener, E. Löwer, R. Ditscherlein, K. Krüger, A. Kwade, U.A. Peuker, 3D ex-situ and in-situ X-ray CT process studies in particle technology—a perspective. Adv. Powder Technol. **31**(1), 78–86 (2020). https://doi.org/10.1016/j.apt.2019.09.038
52. F.E. Boas, D. Fleischmann, CT artifacts: causes and reduction techniques. Imaging Med. **4**(2), 229–240 (2012)
53. F. Bernier, R. Tahara, M. Gendron, Additive manufacturing powder feedstock characterization using X-ray tomography. Met. Powder Rep. **73**(3), 158–162 (2018). https://doi.org/10.1016/j.mprp.2018.01.002
54. A. Sola, A. Nouri, Microstructural porosity in additive manufacturing: the formation and detection of pores in metal parts fabricated by powder bed fusion. J. Adv. Manuf. Process. (2019). https://doi.org/10.1002/amp2.10021

55. T.T. Lam, *High Density Sintering of Iron-Carbon Alloys via Transient Liquid Phase* (California Univ., Berkeley, 1978)
56. L. Collini, G. Nicoletto, R. Konečná, Microstructure and mechanical properties of pearlitic gray cast iron. Mater. Sci. Eng. A **488**(1–2), 529–539 (2008). https://doi.org/10.1016/j.msea.2007.11.070
57. S. Giganto, S. Martínez-Pellitero, J. Barreiro, P. Zapico, Influence of 17–4 PH stainless steel powder recycling on properties of SLM additive manufactured parts. J. Market. Res. **16**, 1647–1658 (2022). https://doi.org/10.1016/j.jmrt.2021.12.089
58. I. Ohnaka et al., Mechanism and estimation of porosity defects in ductile cast iron. Int. J. Cast Met. Res. **21**(1–4), 11–16 (2013). https://doi.org/10.1179/136404608x361585
59. R. Monroe, Porosity in castings. AFS Trans. **113**, 519–546 (2005)